Scripta Materialia 153 (2018) 99–103

Contents lists available at ScienceDirect

Scripta Materialia

journal homepage: www.elsevier.com/locate/scriptamat

Regular article

Early plastic deformation behaviour and energy absorption in porous β-type biomedical titanium produced by selective laser melting

Y.J. Liu [a], S.J. Li [c], L.C. Zhang [b,*], Y.L. Hao [c], T.B. Sercombe [a,*]

[a] School of Mechanical and Chemical Engineering, The University of Western Australia, 35 Stirling Highway, Perth, WA 6009, Australia
[b] School of Engineering, Edith Cowan University, 270 Joondalup Drive, Joondalup, Perth, WA 6027, Australia
[c] Shenyang National Laboratory for Materials Science, Institute of Metal Research, Chinese Academy of Sciences, 72 Wenhua Road, Shenyang 110016, China

ARTICLE INFO

Article history:
Received 21 April 2018
Received in revised form 2 May 2018
Accepted 6 May 2018
Available online xxxx

Keywords:
Selective laser melting
β titanium
Porous structures
Energy absorption
Local stress concentrations

ABSTRACT

Energy absorption is a critical consideration in the design of porous structures design. This work studied the energy absorption mechanism of three porous structures (i.e. cubic, topology optimised and rhombic dodecahedron) at the early stage of deformation. Stress distribution results, obtained by finite element modelling, coupled with the investigation of the slip bands generated have been used to reveal the plasticity mechanism and local stress concentrations for each structure. The topology optimised structure exhibits the best balance of bending and buckling stress with a high elastic energy absorption, a low Young's modulus (~2.3 GPa) and a high compressive strength (~58 MPa).

In addition to their attractive properties such as light weight and high strength, titanium alloys have been widely used as biomaterials due to their relatively low Young's Modulus, good biocompatibility and corrosion resistance [1–3].

Modern additive manufacturing (AM) technologies, such as selective laser melting (SLM) and electron beam melting (EBM), are able to produce the titanium porous implant with properties that mimic those of bone [4–7]. In recent years AM-produced titanium porous parts have attracted considerable research attention [8–18]. For example, Cheng et al. [16] investigated the open cellular structures and reticulated meshes of Ti–6Al–4 V alloy made by EBM and found that the reticulated meshes had a higher specific strength (~113 MPa with the porosity of 62%). Wang et al. [17] concluded that the AM-produced titanium porous structures would play a significant part in future human implants.

Driven by their ultra-low Young's Modulus and high strength, AM-produced β-type titanium alloys containing non-toxic elements have been emerging as the next generation candidate biomaterials [19,20]. Liu et al. [21] found that the SLM-produced β-type Ti-24Nb-4Zr-8Sn (Ti2448) porous specimens with topology optimised structures have good ductility (~14%), high strength (~51 MPa) and a low density (<1 g/cm^3). Furthermore, Ti2448 porous structures exhibit superelasticity, which is known to reduce the fatigue crack growth rate via increasing the size of plastic zone at crack tip [22]. But the shape of porous structure strongly affects the fatigue properties of porous parts. Yavari et al. [23] found that the truncated cuboctahedron structure has a higher fatigue life than the diamond structure at the same normalized applied stress. Zhao et al. [24] concluded that the strut buckling contribution and cyclic ratcheting rate are determined by the cell shape of porous structures, thereby affecting their fatigue properties. Furthermore, Bobbert et al. [25] found that the fatigue limit of porous structures can be improved to 60% of their yield stress by adjusting the unit cell design. A good porous structure can reduce stress concentrations and improve mechanical properties by adjusting bending and buckling deformation and optimizing plastic and elastic energy absorption [26,27].

Although theoretical frameworks have been established for the elastic and plastic deformation of bulk parts, no such a framework currently exists for porous structures based on the analysis of elastic and plastic energy absorption for different unit cell shapes. As such, this work concentrates on super-elasticity, early plasticity and energy absorption in different Ti2448 porous structures made by SLM. The stress distribution and local stress concentration combined with the slip band generation have also been studied.

Magics software (Materialize, Belgium) was used to produce three different 3 × 3 × 3 unit cell structures (cubic, topology optimised [4] and rhombic dodecahedron) using 3.33 × 3.33 × 3.33 mm^3 unit cells (i.e. overall size was 10 × 10 × 10 mm^3) (Fig. 1). Each structure had a nominal porosity of 80% and an as-built porosity of 75%. These porous specimens were then manufactured using SLM in a Realizer SLM100 system, with a layer thickness of 50 μm, an input energy of 200 W and

* Corresponding author.
E-mail addresses: l.zhang@ecu.edu.au, lczhangimr@gmail.com, (L.C. Zhang), tim.sercombe@uwa.edu.au (T.B. Sercombe).

https://doi.org/10.1016/j.scriptamat.2018.05.010
1359-6462/

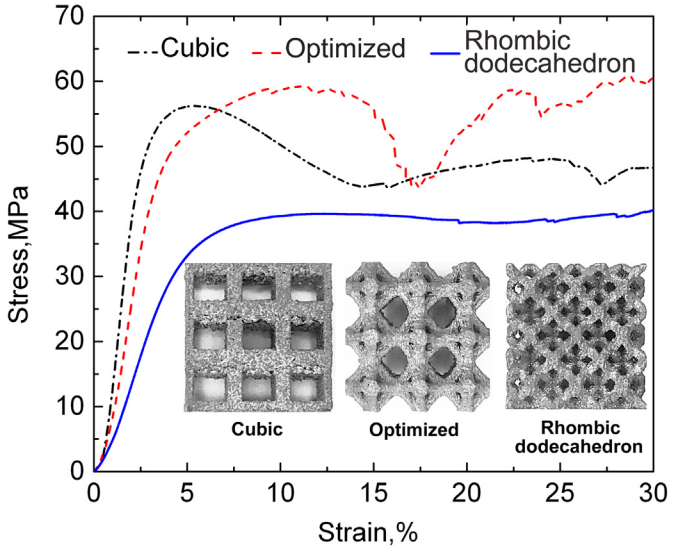

Fig. 1. The typical compressive stress-strain curves for three structures. The insets show SLM-produced samples.

a laser scan speed of 750 mm/s. The powder used was spherical Ti2448 with particle sizes of 45–106 μm, produced using electrode induction melting gas atomization (EIGA). All the samples in this work were processed in a single build. For the microstructural characterization, a specimen of each porous structure was cold mounted in using Struers' Epofix resin. The mounted specimens were ground and polished using standard metallographic procedures and finished with 0.04μm colloidal silica containing 30% hydrogen peroxide. Microstructural features were investigated by scanning electron microscopy (SEM) on a FEI Verios XHR 460 in back-scatted electron (BSE) mode. Compressive tests were performed on three samples for each group using an Instron 5982 machine at a strain rate of 0.1 mm/min. Young's Moduli (E) were measured using the unloading curves. Multiple loading tests from 1% to 6% strain were conducted at the same strain rate. During each test, the specimen was first loaded up to a 1% strain level, completely unloaded and then loaded again to 2% strain. This was continued at 1% step up to 6% strain (i.e. 6-cyclic loading-unloading tests on each sample). Finite element modelling (FEM) was carried out using Comsol 4.2a software. Three different $3 \times 3 \times 3$ unit cell models were used to study the stress distribution. The compressive load was loaded on the top surface of sample paralleled to Z axis (i.e. the build direction). The bottom boundary was fixed in the Z direction to simulate the effect of loading conditions and the rest of the boundaries were set as free, which was similar to the conditions in uniaxial compressive testing.

The typical compressive stress-strain curves for three different structures are shown in Fig. 1. Previous studies showed that similar SLM-produced Ti2448 porous structures consisted of a single β phase [19]. Therefore, it is expected that all three structures should also comprise of a single β phase. Nevertheless, these three structures exhibit different levels of ductility. The topology optimised and cubic structures have a similar first maximum compressive strength (~58 MPa and ~56 MPa, respectively). However, they undergo a very different deformation strain before the first layer-wise failure occurs, with a value of ~15% and ~6% respectively. Zhao et al. [24] showed that in porous structures, the unit cell design affects the properties depending on the relative contribution of bending and buckling. For example, the cubic structure displays low ductility because the deformation is dominated by buckling; while under the same loading condition, the deformation in the topology optimised structure is determined by both bending and buckling. As the struts of cubic structure are parallel to loading direction, there is little bending stress; while the angle between the struts of topology optimised structure and loading direction is 45° [2], the topology optimised structure has higher bending stress than the cubic

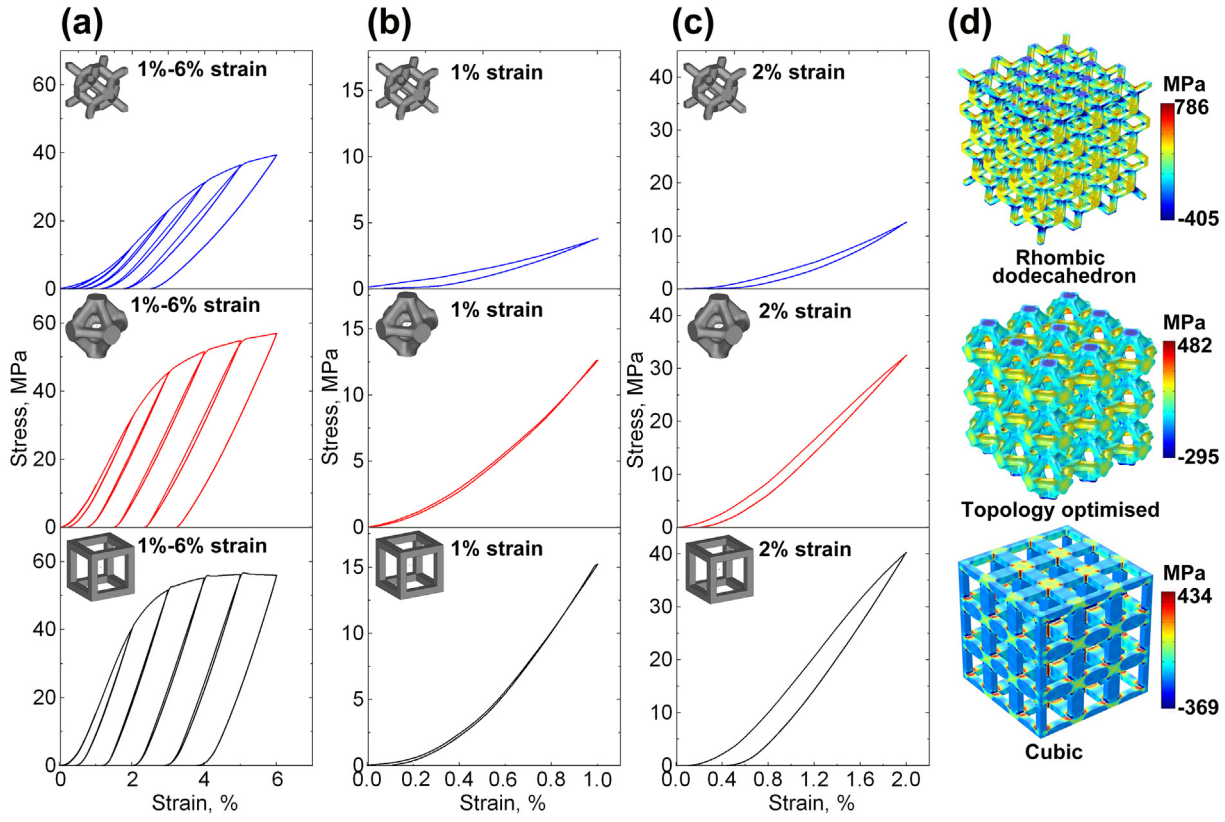

Fig. 2. The stress-strain curves for multiple cyclic load-unloading curves and FEM results for three structures: (a) the stress-strain curves at a range of 1–6% strain levels, (b) the stress-strain curves at 1% strain level, (c) the stress-strain curves at 2% strain level and (d) the FEM stress distribution at 1% strain level.

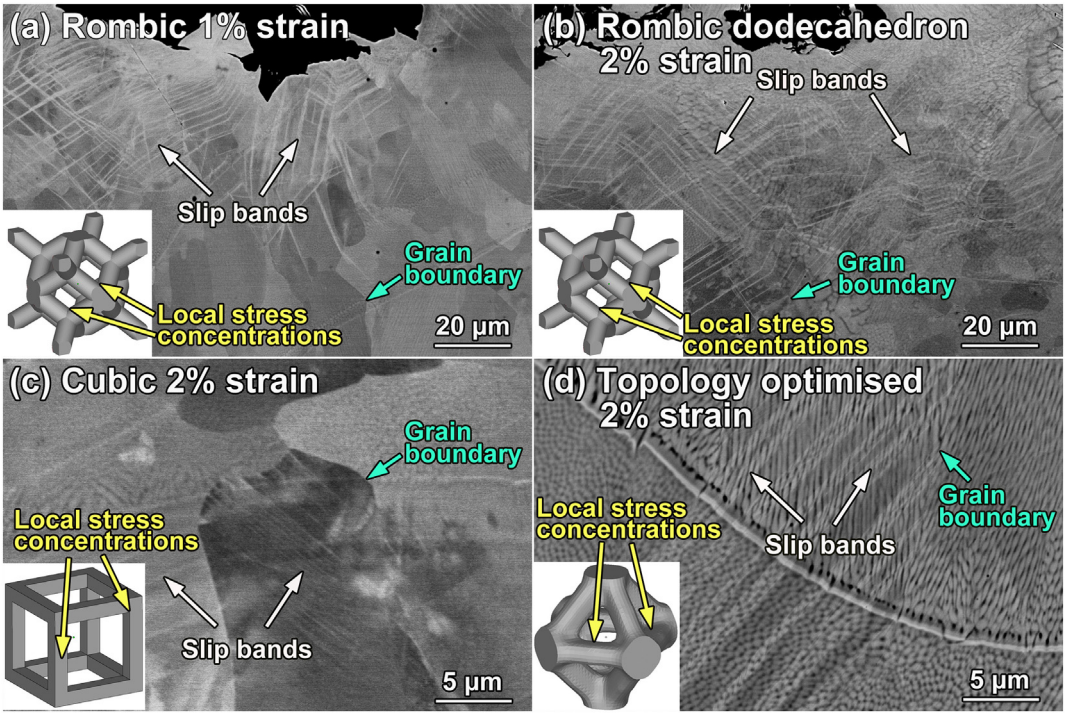

Fig. 3. The SEM-BSE images for the slip bands in three structures at different strain levels: (a) the rhombic dodecahedron sample at 1% strain level, (b) the rhombic dodecahedron sample at 2% strain level, (c) cubic sample at 2% strain level, and (d) the topology optimised sample at 2% strain level.

structure. As bending contributes more to deformation, the topology optimised structure undergoes more deformation than the cubic structure. Contrary to the cubic structure, the deformation of rhombic dodecahedron structure is affected more by bending [24]. Clearly, there is no evident layer-wise failures in rhombic dodecahedron structure, therefore it displays the best ductility (> 30%) but the lowest strength (~40 MPa) among the three structures.

The multiple loading-unloading curves for three groups of structures are shown in Fig. 2. All the sample groups were subjected to cyclic uniaxial compressive loading with a gradually increasing total strain. The

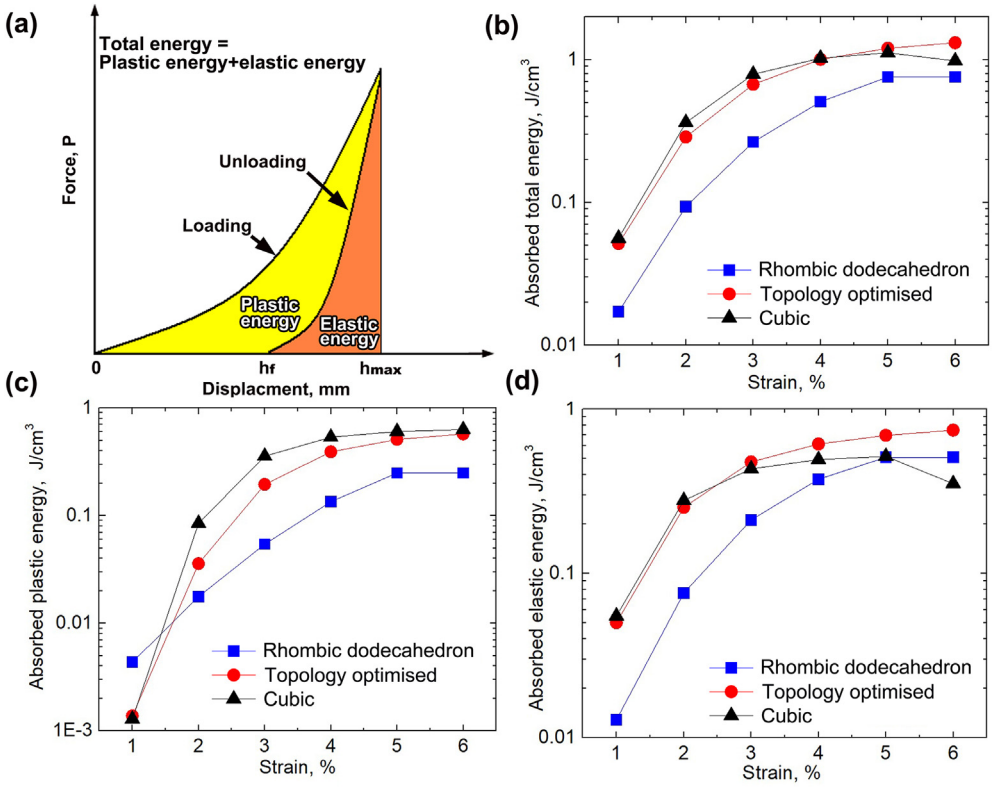

Fig. 4. The energy absorption for three groups: (a) the diagrammatic sketch of energy absorption, (b) the total energy absorption, (c) the plastic energy absorption, and (d) the elastic energy absorption.

Table 1
Compressive mechanical properties and phase constituents of additive manufactured titanium materials. EBM: electron beam melting; SLM: selective laser melting; *E*: Young's modulus and σ_{max}: maximum compressive strength.

Material	Unit shape	Method	Porosity (%)	Phase constituent	*E* (GPa)	σ_{max} (MPa)	Refs
Ti2448	Solid	SLM	–	β	~53 ± 1	665 ± 18	[28]
Ti2448	G7 (Magics)	EBM	70	α + β	~0.7 ± 0.1	35 ± 2	[30]
Ti6Al4V	Dodecahedron	SLM	75	α + β	~1.40	~42.8	[31]
Ti6Al4V	Rhombic dodecahedron	EBM	75	α + β	~2	~40	[32]
Ti2448	Rhombic dodecahedron	SLM	75	β	~1.13	~40	This work
Ti2448	Topology optimised	SLM	75	β	~2.3	~58	This work
Ti2448	Cubic	SLM	75	β	~3.3	~56	This work

results show that these groups of samples have different recovery abilities. In addition to the effect of the structure, the single β phase and super-elasticity of Ti2448 alloy also contribute to the recovery ability [22]. The rhombic dodecahedron structure exhibits a strong resilience at 6% strain (Fig. 2 (a)). But this structure exhibits a small amount of plastic strain after the first loading-unloading cycle (Fig. 2 (b)). Moreover, the area, over which slip bands form, increases with the increment in cyclic strain level, that is the amount of slip bands at 2% cyclic strain is greater than at 1% cyclic strain (Figs. 3 (a) and (b)). It is apparent that the slip bands are concentrated at both the top and bottom of the node in rhombic dodecahedron structure. The other two structures do not exhibit significant plastic strain until after second loading-unloading cycle at 2% strain (Fig. 2 (c)) and regions with high stress concentration (indicated by the yellow arrows in Fig. 3 (c) and (d)) are formed in the structures. FEM analysis (Fig. 3 (d)) provides insight into the stress distribution for three structures under compression and reveals the dominant causes for such a difference in mechanical behaviour. Clearly, the local stress is high at the node of rhombic dodecahedron structure. The maximum stress of the rhombic dodecahedron structure at 1% strain is ~786 MPa, which is not only higher than that of the other two structures (482 MPa and 434 MPa for the topology optimised and cubic structure, respectively), but also exceeds the strength of the material (~665 MPa [28]). Figs. 3(b)–(d) show the slip bands generated and their location after 2% cyclic strain. It is apparent that these are forming in areas of high stress as predicted by the FEM analysis (Fig. 2 (c)).

One of the key attributes of a porous structure is to absorb energy when the stress and strain are less than the design limits [29]. For a given porous structure, the total energy absorbed from displacement 0 to h_{max} can be calculated from [29]:

$$W_T = \int_0^{h_{max}} P(h)\mathrm{d}h \tag{1}$$

where W_T is the total energy absorption and P is the loading force. The elastic energy absorbed during the same deformation is given by:

$$W_E = \int_{h_f}^{h_{max}} P(h)\mathrm{d}h \tag{2}$$

where W_E is the elastic energy absorption and h_f is the displacement after unloading. The plastic energy absorption W_P is then calculated by:

$$W_P = W_T - W_E \tag{3}$$

This is shown schematically in Fig. 4 (a). At a given strain level, a higher maximum stress results in higher total energy absorption, which consists of both elastic and plastic energy absorption. The plastic energy absorption is mainly a result of the generation and movement of dislocations or/and slip bands. Higher elastic energy absorption results in better recovery after unloading. In Figs. 4 (b)-(d), total energy absorption, plastic energy absorption and energy absorption for three structures are given under different strain levels ranging from 1% to 6%. It is clear that the rhombic dodecahedron structure exhibits the lowest total energy absorption, as it has the lowest maximum stress for each cycle. The rhombic dodecahedron structure exhibits the highest absorbed plastic energy after the first cycle, which results from the high local stress concentrations causing yielding at this strain (Fig (b) and (d)). However, at higher strains, it has the lowest absorbed plastic energy (Fig. 4 (c)). The topology optimised and cubic groups have a similar total energy absorption but a different plastic and elastic energy absorption. Specifically, the topology optimised structure presents a lower plastic and higher elastic energy absorption compared with the cubic structure. Table 1 compares the mechanical properties including Young's Modulus and maximum compressive strength for different structures produced by both EBM and SLM using different materials. The properties of the porous structures can be adjusted by changing the unit shape to achieve optimal mechanical properties. An ideal structure should meet the requirements of high strength, low Young's modulus and high elastic recovery ability. Comparison of the structures in current and previous work reveals that the topology optimised structure is best in terms of all these properties.

In summary, the difference in energy absorption for the three structures studied is primarily a result of the difference in stress distribution and local stress concentrations. The local stress concentrations were analyzed using finite element modelling, and the generation of slip bands associated with plastic energy absorption in different structures has been studied after different strain levels using cyclic loading-unloading test. The topology optimised structure is identified as an interesting candidate for future implant applications due to its high energy absorption ability.

Acknowledgement

The authors would like to thank W.T. Hou for technical assistance. This work was supported partially by Australian Research Council Discovery Project (DP110101653, DP170104307), Chinese MoST (2016YFC1102601, 2017YFC1104901), Key Research Program of Frontier Sciences, CAS (QYZDJ-SSW-JSC031-02) and National Natural Science Foundation of China (51631007).

References

[1] M. Long, H.J. Rack, Biomaterials 19 (1998) 1621–1639.
[2] T.B. Sercombe, X. Xu, V.J. Challis, R. Green, S. Yur, Z. Zhang, L.P.D, Mater. Des. 67 (2015) 501–508.
[3] L.C. Zhang, Y. Liu, S. Li, Y. Hao, Adv. Eng. Mater. (2017)https://doi.org/10.1002/adem.201700842.
[4] V.J. Challis, A.P. Roberts, J.F. Grotowski, L.C. Zhang, T.B. Sercombe, Adv. Eng. Mater. 12 (2010) 1106–1110.
[5] D.D. Gu, W. Meiners, K. Wissenbach, R. Poprawe, Int. Mater. Rev. 57 (2012) 133–164.
[6] H. Attar, L. Löber, A. Funk, M. Calin, L.C. Zhang, K.G. Prashanth, S. Scudino, Y.S. Zhang, J. Eckert, Mater. Sci. Eng. A 625 (2015) 350–356.
[7] Y.J. Liu, Z. Liu, Y. Jiang, G. Wang, Y. Yang, L.C. Zhang, J. Alloys Compd. 735 (2018) 1414–1421.
[8] B. Van Hooreweder, Y. Apers, K. Lietaert, J.-P. Kruth, Acta Biomater. 47 (2017) 193–202.
[9] L.C. Zhang, H. Attar, Adv. Eng. Mater. 18 (2016) 463–475.
[10] V.J. Challis, X. Xu, L.C. Zhang, A.P. Roberts, J.F. Grotowski, T.B. Sercombe, Mater. Des. 63 (2014) 783–788.
[11] Y. Chen, J. Zhang, N. Dai, P. Qin, H. Attar, L.C. Zhang, Electrochim. Acta 232 (2017) 89–97.

[12] N. Dai, L.C. Zhang, J. Zhang, X. Zhang, Q. Ni, Y. Chen, M. Wu, C. Yang, Corros. Sci. 111 (2016) 703–710.
[13] N. Dai, L.C. Zhang, J. Zhang, Q. Chen, M. Wu, Corros. Sci. 102 (2016) 484–489.
[14] Q. Wang, R. Ling, x.P. Li, S. Zhang, Y.T.B. Sercombe, K. Yang, Mater Sci Eng, C 68 (2016) 519–522.
[15] W. Xu, M. Brandt, S. Sun, J. Elambasserl, Q. Liu, K. Latham, K. Xia, M. Qian, Acta Mater. 85 (2015) 74–84.
[16] X.Y. Cheng, S.J. Li, L.E. Murr, Z.B. Zhang, Y.L. Hao, R. Yang, F. Medina, R.B. Wicker, J. Mech. Behav. Biomed. Mater. 16 (2012) 153–162.
[17] D. Wang, Y. Yang, R. Liu, D. Xiao, J. Sun, J. Mater. Process. Technol. 213 (2013) 1734–1742.
[18] Z.G. Karaji, R. Hedayati, B. Pouran, I. Apachitei, A.A. Zadpoor, Mater. Sci. Eng. C 76 (2017) 406–416.
[19] Y.J. Liu, S.J. Li, H.L. Wang, W.T. Hou, Y.L. Hao, R. Yang, T.B. Sercombe, L.C. Zhang, Acta Mater. 113 (2016) 56–67.
[20] S. Ehtemam-Haghighi, Y.J. Liu, G. Cao, L.C. Zhang, Mater. Sci. Eng. C. 60 (2016) 503–510.
[21] Y.J. Liu, X.P. Li, L.C. Zhang, T.B. Sercombe, Mater. Sci. Eng. A 642 (2015) 268–278.
[22] Y.J. Liu, H.L. Wang, S.J. Li, S.G. Wang, W.J. Wang, W.T. Hou, Y.L. Hao, R. Yang, L.C. Zhang, Acta Mater. 126 (2017) 58–66.
[23] S.A. Yavari, S. Ahmadi, R. Wauthle, B. Pouran, J. Schrooten, H. Weinans, A. Zadpoor, J. Mech. Behav. Biomed. Mater. 43 (2015) 91–100.
[24] S. Zhao, S. Li, W. Hou, Y. Hao, R. Yang, R. Misra, J. Mech. Behav. Biomed. Mater. 59 (2016) 251–264.
[25] F. Bobbert, K. Lietaert, A.A. Eftekhari, B. Pouran, S. Ahmadi, H. Weinans, A. Zadpoor, Acta Biomater. 53 (2017) 572–584.
[26] S. Babaee, B.H. Jahromi, A. Ajdari, H. Nayeb-Hashemi, A. Vaziri, Acta Mater. 60 (2012) 2873–2885.
[27] R. Hedayati, M. Sadighi, M. Mohammadi-Aghdam, A. Zadpoor, Mater Sci Eng, C 60 (2016) 163–183.
[28] L.C. Zhang, D. Klemm, J. Eckert, Y.L. Hao, T.B. Sercombe, Scripta Mater. 65 (2011) 21–24.
[29] U.E. Ozturk, G. Anlas, Mater. Des. 30 (2009) 15–22.
[30] Y.J. Liu, S. Li, W. Hou, S. Wang, Y. Hao, R. Yang, T.B. Sercombe, L.C. Zhang, J. Mater. Sci. Technol. 32 (2016) 505–508.
[31] S.A. Yavari, R. Wauthlé, J. van der Stok, A. Riemslag, M. Janssen, M. Mulier, J.-P. Kruth, J. Schrooten, H. Weinans, A.A. Zadpoor, Mater Sci Eng., C, 33 (2013) 4849–4858.
[32] S. Li, Q. Xu, Z. Wang, W. Hou, Y. Hao, R. Yang, L. Murr, Acta Biomater. 10 (2014) 4537–4547.